Math Geosci (2020) 52:593–617
https://doi.org/10.1007/s11004-019-09825-5

# Geological Facies Recovery Based on Weighted $\ell_1$-Regularization

**Hernan Calderon[1] · Felipe Santibañez[1] · Jorge F. Silva[1] · Julián M. Ortiz[2] · Alvaro Egaña[3]**

Received: 29 January 2018 / Accepted: 26 August 2019 / Published online: 18 September 2019


**Abstract** A weighted compressed sensing (WCS) algorithm is proposed for the problem of channelized facies reconstruction from pixel-based measurements. This strategy integrates information from: (i) image structure in a transform domain (the discrete cosine transform); and (ii) a statistical model obtained from the use of multiple-point simulations (MPS) and a training image. A method is developed to integrate multiple-point statistics within the context of WCS, using for that a collection of weight definitions. In the experimental validation, excellent results are reported showing that the WCS provides good reconstruction for geological facies models even in the range of [0.3–1%] pixel-based measurements. Experiments show that the proposed solution outperforms methods based on pure CS and MPS, when the performance is measured in terms of signal-to-noise ratio, and similarity perceptual indicators.

✉ Felipe Santibañez
fsantibanez@uchile.cl
http://www.ids-uchile.cl

Hernan Calderon
hcalderon@ing.uchile.cl

Jorge F. Silva
josilva@ing.uchile.cl

Julián M. Ortiz
julian.ortiz@queensu.ca

Alvaro Egaña
aegana@alges.cl

1 Information and Decision System Group (IDS), Department of Electrical Engineering, University of Chile, Av. Tupper 2007, 837-0451 Santiago, Chile

2 The Robert M. Buchan Department of Mining, Queen's University, Kingston, ON, Canada

3 Advanced Mining Technology Center (AMTC), Santiago, Chile

**Keywords** Channelized facies images · Image synthesis and reconstruction · Sparse promoting reconstruction · Weighted compressed sensing · Multiple-point statistics · Geostatistics

## 1 Introduction

The problem of geological facies recovery from pixel-based measurements is a challenging topic in Geosciences. Direct measurements (hard-data or pixel based measurements) are expensive, and consequently, the inverse problem needs to be addressed in an extreme under-sampling regime (Mariethoz and Caers 2015). Typically, a realistic scenario considers less than 3% of direct measurements. To deal with this challenging under-sampling regime, the use of non-parametric models for statistical simulation is a well-established approach (Ortiz and Deutsch 2004).

In particular, multiple-point simulations (MPS) have been adopted as a standard method in geostatistics (Guardiano and Srivastava 1993; Strebelle 2002; Ortiz and Deutsch 2004; Arpat and Caers 2007; Wu et al. 2008; Mariethoz and Caers 2015; Minniakhmetov et al. 2018). Conditioned to the direct measurements, this approach simulates the variables in un-sampled locations by reproducing higher order patterns (multiple-point statistics) of a prior model obtained from a training image (Mariethoz and Caers 2015). An expert can then translate the prior knowledge in the selection of an appropriate training image from which reference spatial patterns are drawn and imposed during the reconstruction. This is a stochastic approach in which the variability in the results is intrinsic, in the sense that it does not lead to a single reproduction of the distribution of facies. More recently other models have been proposed for image reconstruction, including Markov-process based (Tahmasebi et al. 2017) and Deep Learning methods based on Convolutional Neural Networks (Wang et al. 2018). Finally, the problem of image recovery has also been addressed as a sampling problem (Jafarpour et al. 2009; Calderon et al. 2015) by adopting some new results from the theory of compressed sensing (CS) (Candès and Tao 2005, 2006; Candès et al. 2006a, b; Donoho 2006). These approaches depart from the classical strategy of image recovery based on simulations (Ortiz and Deutsch 2004; Tahmasebi et al. 2014; Mariethoz and Renard 2010; Mariethoz and Lefebvre 2014), and treat image recovery as an interpolation problem (Vetterli and Kovacevic 1995; Donoho et al. 1998; Mallat 2009).

The basic idea of the CS framework is to optimize signal recovery by taking advantage of the fact that subsurfaces facies images have a redundant representation in a transform domain, that is they have less effective degrees of freedom than the dimensionality of the image (the concept of sparsity). Sparseness or compressibility is the ability of an image to be perfectly or well approximated by a small fraction of transform coefficients. CS exploits (Candès et al. 2006a; Donoho 2006) sparsity to recover the image with the minimum number of non-zero coefficients for a given transform domain. In this sampling context, performance is measured by a comparison between the true image and that of the recovered image (Donoho et al. 1998; Vetterli and Kovacevic 1995; Elad 2010) using distortion measures such as the signal to noise ratio (SNR) or visual perceptual indicators (Zhou et al. 2004), widely adopted by the

community of image compression. In contrast, the conventional way of evaluating the quality of geostatistical simulations has been based on assessing the reproduction of univariate, bivariate and multiple-point statistics of an image model (Ortiz and Deutsch 2004; Mariethoz and Renard 2010; Tan et al. 2014; Peredo and Ortiz 2011; Leuangthong et al. 2004).

The application of CS to inverse problems in Geosciences is an active area of research. In particular, there are several contributions to the problem of subsurface flow model calibration based on non-linear flow measurements (Jafarpour et al. 2010; Jafarpour 2011; Khaninezhad et al. 2012; Elsheikh et al. 2013; Khaninezhad and Jafarpour 2014, 2017; Lee and Kitanidis 2013). These contributions have been made in the context of History Matching (Jung et al. 2018, 2017; Khaninezhad and Jafarpour 2017; Lee et al. 2017, 2016; Sana et al. 2015; Jafarpour 2011). History Matching is an inference task that incorporates production information and the use of flow-dynamic models that take into account physical parameters of the problem (static parameters, permeability and porosity, and dynamic variables, pressure and saturation, and so on) to recover a subsurface image (Sana et al. 2015, 2016; Li and Jafarpour 2009; Khaninezhad et al. 2012). These works support the idea that sparsity-promoting solutions improve connectivity in the reconstruction of channelized structures and, consequently, improve performance. In the context of geological facies recovery without the use of secondary models or historical data, pixel-based measurements have been used to explore the role of CS for the channelized facies recovery (Jafarpour et al. 2009). This approach focused on the analysis of a single-channel structure and a specific data-rate regime, showing promising results. Calderon et al. (2015) extended this direction addressing the formal connections with the *RIPless theory* of CS (Candès and Plan 2011), formulating the problem of basis selection and proposing a new inter-block average approach for processing arbitrary large images. They performed a systematic experimental analysis in the range of [1–10%] of direct data, showing that CS is an interesting alternative for facies reconstruction when more than 3% of the data is available.

In many realistic situations less than 1% of pixel-based measurements are available. In this severe under-sampling regime, the aforementioned method (Jafarpour and McLaughlin 2009) and the average inter-block CS approach (Calderon et al. 2015) are limited. To address the problem of facies reconstruction with such limitations, a new framework is proposed in this work by integrating knowledge of the structure of the facies image in a transform domain (the Discrete Cosine Transform) with the statistical information obtained from the multiple-point statistics of a training image. The main conjecture is that these two sources of subsurface image information are complementary and, consequently, their integration can provide a significant improvement in the reconstruction results. In order to validate this hypothesis, the use of weighted CS (WCS) is explored as a concrete alternative to integrate information from a statistical model of the image (or image model) within the umbrella of sparsity promoting solutions in a transform domain (Figueiredo and Nowak 2014; Bogdan et al. 2013; Zeng and Figueiredo 2014; Khajehnejad et al. 2011).

WCS is an active area of research in signal processing where the objective is to incorporate prior statistical information of the signal for better recovery (Figueiredo

and Nowak 2014; Bogdan et al. 2013). Empirical results have shown outstanding performance in the recovery of sparse signals, significantly outperforming the classical CS framework (Khajehnejad et al. 2011; Zeng and Figueiredo 2014). On the theoretical side, there have been some concrete contributions (Figueiredo and Nowak 2014; Khajehnejad et al. 2011). For instances, the use of WCS for sparse estimation of correlated variables has been studied (Figueiredo and Nowak 2014), establishing theoretical upper-bounds for estimation error. With these upper-bounds, the use of prior statistical information from theory and practice can offer an important gain in image reconstruction.

Motivated by these results on signal processing, a new inter-block average reconstruction approach is presented based on WCS that integrates signal structure and statistical knowledge from a training image. To this end, a formalization to integrate information of a training image in a weighted structure within the context of WCS is provided. In terms of performance, the proposed approach provides important improvements when compared with the pure CS-based solution (Calderon et al. 2015). This gain is clear in the critical regime [0.1–0.8%] of pixel-based measurements considering three different image models (single-channel, multi-channel 1 and multi-channel 2). Furthermore, a comparison of the proposed schemes with MPS is performed verifying that from the point of view of recovering the actual image (using SNR and perceptual indicators) WCS performs better in the range [0.1–2%] of pixel-based measurements.

In the areas of computer vision and image processing, similar recovery problems have been addressed. Here, the setting resembles an ill-posed problem known as image inpainting where the objective is to recover images with contaminated or lost pixels (Ji et al. 2017; Xu and Yin 2016; Huang et al. 2008; Srinivas et al. 2015). More generally, a classic problem of image deconvolution (called blind deconvolution) is to restore a blurred or distorted image assuming that samples come from the convolution of a *real* latent source with an unknown blurring kernel (Perrone and Favaro 2016). In this context, Bayesian models have become a natural alternative as prior information is included in the framework. Classical Bayesian works include modeling priors with a variety of tools. These include modeling with conditional autoregression (CAR) or simultaneous autoregression (SAR) using a Dirichlet prior to model the blur kernel (Molina et al. 1997), and with the mixture of Laplacians (Miskin and MacKay 2001) or Gaussians priors (Likas and Galatsanos 2004) to impose smoothness on the image. In addition, blur kernels and total variation have been used to impose piecewise-smoothness (Perrone and Favaro 2014, 2016; Rudin et al. 1992; Likas and Galatsanos 2004; Chen et al. 2014; Babacan et al. 2009). Since the work of Fergus et al. (2006), sparse prior modeling on the blurring kernel have become the state-of-the-art (Amizic et al. 2010; Babacan et al. 2009; Vega et al. 2014). On the non-Bayesian side, fast $\ell_p$-regularization schemes for sparse deconvolution have been proposed (Zhou et al. 2014). However, Choudhary and Mitra (2014) showed that on a single channel scenario, the assumption of sparsity in the canonical basis is not sufficient to ensure identifiability. On the other hand, although using a highly structured regularization setting, the number of samples needed for a good deconvolution, even for small images, can be impractical (Zhang et al. 2018).

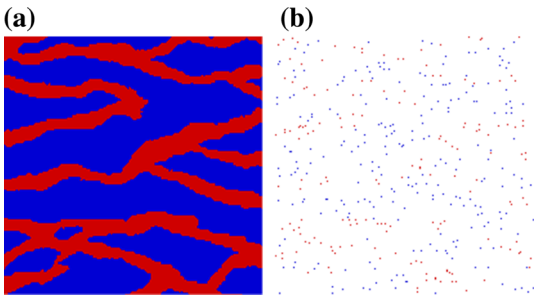


**Fig. 1** **a** A multichannel facies image. **b** Unstructured pixel-based measurements (1% taken at random positions). White pixels indicate the absence of measurements

The rest of the paper is organized as follows. Section 2 presents the formulation of the facies recovery problem in the context of CS and discusses about some design considerations. Section 3 presents the weighted CS framework used to integrate the two sources of prior information available for the geological facies. Finally, Sect. 4 analyzes the persistent structure of facies images in the DCT transform domain, and Sect. 5 presents reconstruction results and comparison with other methods.

## 2 Facies Recovery Using Compressed Sensing

The main problem of this work is the recovery of a geological structure acquired from wells considering the distributions of two-dimensional facies over a deposit or reservoir illustrated in Fig. 1a. This problem is modeled as the recovery of an image (a collection of pixels $(x_{i,j}) \in \mathbb{R}^{\{1,\ldots,N\}\times\{1,\ldots,N\}}$ indexed by the pair $(i, j) \in \{1, \ldots, N\}\times\{1, \ldots, N\}$), where the wells correspond to unstructured pixel measurements of a small proportion of the image size in the range [0.1–2%], see Fig. 1b for an illustration.

### 2.1 Compressed Sensing: A Transform-Based Sparsity Promoting Solution

In this work, the focus is on the sampling regime of [0.1–2%] to perform image reconstruction. In this extreme under-sampling regime, any classical interpolation or sampling algorithm perform poorly. Therefore, the use of concrete models for the structure of the image is essential to achieve a reasonable recovery from the observations.

Without loss of generality, an image is represented by a finite vector $x$ in $\mathbb{R}^n$, where the pixel-based measurements are represented as a linear operator, that is,

$$\bar{y} = A\bar{x} \in \mathbb{R}^m. \tag{1}$$

In the Eq. (1), the $m$ by $n$ matrix, $A$, models the sensing process where $m$ represents the number of samples and $n$ the dimension of the image. The observation vector is denoted by $\bar{y}$. Here, the measurements (the rows of $A$) are taken at random pixel locations to model the sensing strategy. In particular, the rows of $A$ are produced as independent and identically distributed (i.i.d.) realizations of a random vector $\bar{a}(w)$ in $\mathbb{R}^n$, which independently takes (without repetitions) $m$ -columns of the identity matrix

$I$ with uniform probability to form the $m$-rows of $A$ in (1). To illustrate the process, an example of the induced structure of $A$ is presented in Fig. 1b.

For the under sampling regime (i.e., $m \ll n$), the recovery of $\bar{x}$ from $\bar{y}$ is an ill-posed problem. However under some specific structural assumptions on $\bar{x}$, the CS theory suggests it is feasible to obtain perfect or near-optimal reconstruction (Candès and Tao 2005; Candès et al. 2006b; Donoho 2006; Cohen et al. 2009). Formally, let $U$ be an unitary matrix (i.e. the columns of $U$ define an orthonormal basis for $\mathbb{R}^n$), then the signal $\bar{x} \in \mathbb{R}^n$ can be expressed by

$$\bar{x} = U\bar{z}, \tag{2}$$

where $\bar{z} \equiv U^{\dagger}\bar{x}$ denotes the *transform representation* of $\bar{x}$ with respect to $U$. Hence, (1) can be expressed as

$$\bar{y} = AU \cdot \bar{z} \in \mathbb{R}^m, \tag{3}$$

relating the pixel-based measurements $\bar{y} \in \mathbb{R}^m$ with the transform coefficients $\bar{z} \in \mathbb{R}^n$ (with respect to $U$). It can be shown (more details in Calderon et al. 2015, Sects. 2 and 3 and "Appendix A") that if the transform vector $\bar{z}$ is $k$-sparse, meaning that the vector $\bar{z}$ has at most $k$ non-zero coefficients and $k \ll n$, perfect reconstruction of $\bar{x}$ can be obtained from $\bar{y}$ with the following transform-based *sparsity promoting solution* (Candès et al. 2006b; Donoho 2006; Candès and Plan 2011)

$$\hat{z} = \arg\min_{\tilde{z}\in\mathbb{R}^n} ||\tilde{z}||_{\ell_1}, \quad \text{subject to } \bar{y} = AU\tilde{z}. \tag{4}$$

Finally, from $\hat{z}$, the reconstruction obtained in the pixel (or image) domain is given by the synthesis equation $\hat{x} = U\hat{z}$.

In a nutshell, the underling idea on using the algorithm in (3) to recover the image is that minimizing the $\ell_1$-norm in the transform domain [subject to the linear constraint in (4)] promotes a solution that is both sparse (in the transform domain given by $U$) and consistent with the measurements. Figure 2b illustrates the principle of the recovery algorithm. Remarkably, the solution $\hat{x}$ is equal to $\bar{x}$ when $\bar{z}$ (i.e., the image in the

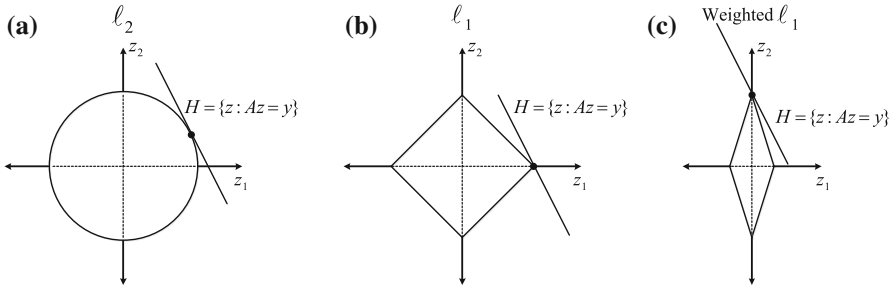


**Fig. 2** Graphical illustration of different solutions (the dot) that can be obtained from a set of linear constraints. **a** Minimizing the $\ell_2$-norm. **b** Minimizing the $\ell_1$-norm. **c** Minimizing the weighted $\ell_1$-norm in Eq. (5), promoting axis $z_2$

transform domain) is sparse, meaning that the number of non-zero coefficients in $\bar{z}$ is significantly smaller than the ambient dimension $n$. For completeness, the CS result that is applicable in the proposed setting is presented in "Appendix A".

### 2.2 Basis Selection for Eq. (4)

In the expression in Eq. (4), the basis $U$ (that models the domain where the image is sparse or nearly sparse) is a design object that needs to be selected with the objective of maximizing the information from $\bar{y}$ that can be used to recover $\bar{x}$, in the linear setting from Eq. (1) and with the algorithm presented in Eq. (4). This poses the problem of finding an optimal basis $U$ over a collection of possibilities (the dictionary). Following the formalization for this selection task presented in Calderon et al. (2015), the optimal basis $U^*$ over a rich collection (DCT, Fourier, Wavelets, etc.) turns out to be the discrete cosine transform (DCT). Some of the technical details of this basis selection problem are presented in "Appendix B".

## 3 Sparse Regularization with Prior Knowledge Support: Weighted CS

The main objective of this work is to propose a strategy to integrate structure in the form of sparsity patterns (on $\bar{z} = U^{\dagger}\bar{x}$) and the statistical information of a channelized facies model. Channelized facies fields present specific spatial features that translate in properties on their spatial correlations, connectivity, orientation, continuity and compressibility patterns, among others. Different realizations of the field are expected to yield a persistent structure in the DCT domain in its transform-based representation. This persistent pattern in the transform domain is a knowledge that can be included in the inverse process in Eq. (4), by favoring solutions that are consistent with an expected geological structure represented in a transform domain.

Within the context of $\ell_1$-regularized solutions, an attractive alternative to integrate prior information is to penalize components in the transform domain that are not consistent with a prior statistical model. This penalization can be modeled through a set of weights $\{w_i\}_{i=1}^n$ in the regularization term (Figueiredo and Nowak 2014; Bogdan et al. 2013). More precisely, the weighted CS synthesis solution is given by

$$\hat{z} = \arg\min_{\tilde{z}\in\mathbb{R}^n} \sum_{i=1}^{n} w_i \, |\tilde{z}_i| = \arg\min_{\tilde{z}\in\mathbb{R}^n} ||W\,\tilde{z}||_1 \quad s.t.\ \bar{y} = A\tilde{z}, \tag{5}$$

where $W = \mathrm{diag}(w_1, w_2, \ldots, w_n)$. Then, the recovered image is computed by $\hat{x} = U\hat{z}$. The criterion for the weights is that $w_i$ should be inversely proportional to the expected magnitude of $z_i$ (Candès et al. 2008). Thus, components with small expected values (irrelevant coefficients in average) will present a high penalization term in Eq. (5), and consequently, the solution of the Eq. (5) will shrink these values to zero. Geometrically, this approach deforms the standard $\ell_1$-ball favoring some sparse orientation patterns as illustrated in Fig. 2c. In summary, the penalization matrix $W$ induces an extra restriction on the space of admissible solutions, penalizing sparse

solutions that fitting the measurements do not honor the prior model imposed by the weights in $W$.

### 3.1 Reducing the Weighted CS to a Standard $\ell_1$-Regularization

The algorithms available to solve the standard sparse regularization inverse problems do not incorporate the weighting matrix $W$ (Elad 2010). This is not an issue since the weighted CS problem reduces to the standard CS algorithm by incorporating $W$ as a modification of the sensing matrix $A$. Specifically, considering a weighted transform domain given by the mapping $\alpha = WU^{\dagger}\bar{x}$, then the problem described in (5) is equivalent to solving

$$\hat{\alpha} = \arg\min_{\tilde{\alpha}\in\mathbb{R}^n} ||\tilde{\alpha}||_1 \quad s.t. \quad \bar{y} = AW^{-1}\tilde{\alpha}, \tag{6}$$

where the recovered image is computed by $\hat{x} = UW^{-1}\hat{\alpha}$ (Candès et al. 2008). There are well-documented algorithms available to solve (6) based on linear programming (basis pursuit) (Elad 2010) as well as greedy iterative solutions with performance guaranteed (orthogonal matching pursuit, iterative-hard thresholding, among others) (Mallat and Zhang 1993; Tropp and Gilbert 2007; Blumensath and Davies 2009; Elad 2010).

### 3.2 Weight Definitions

In this section, a statistical model of a channelized facies field (i.e., the image model) is included within the context of the weighted CS in (5). More formally, the image is modeled as a random vector $X$ with values in $\mathbb{R}^n$ following a distribution $\gamma$. Given the transform-based random vector $Z = U^{\dagger}X$, the computation of the average magnitude of the $i$ coefficient in the transform domain can be obtained by

$$\xi_i = \mathbb{E}(|Z_i|) = \mathbb{E}_{X\sim\gamma}\left(\left|U_{\cdot i}^{\dagger}X\right|\right), \tag{7}$$

for all $i \in \{1,\ldots,n\}$. Considering some recently proposed weighted and reweighted sparse promoting algorithms (Bondell and Reich 2008; Zeng and Figueiredo 2014; Bogdan et al. 2013; Figueiredo and Nowak 2014), a basic design principle is to select $w_i = g(\xi_i)$, where $g : \mathbb{R}\to\mathbb{R}$ is a non-increasing function. In Particular, some definitions from (Zhao and Li 2012) are adopted while others are extended from those. The complete list explored in this work is presented in Table 1. For the case of Definitions 6 and 7, $\Gamma_p \subset \{1,\ldots,n\}$ denotes the set of indices in the transform domain that contain the $p$-most significant coefficients of the average transform representation $\{\xi_i : i = 1,\ldots,n\}$ in Eq. (7).

In practice, there is no access to the probability model $\gamma$. Instead, a training image is used as the model that in the context of the MPS technique offers

**Table 1** List of weighting matrix definitions considered for the solutions of the weighted compressed sensing problem in Eq. (6)

| Name | Definition |
|---|---|
| Definition 1 | $\frac{1}{\xi_i^{1-p}}, \quad 0 < p < 1$ |
| Definition 2 | $\frac{p + \xi_i^{1-p}}{\xi_i^{1-p}(\xi_i + \xi_i^p)}, \quad 0 < p < 1$ |
| Definition 3 | $\frac{p + \xi_i^{1-p}}{\xi_i^{1-p}(\xi_i + \xi_i^p)^{1-p}}, \quad 0 < p < 1$ |
| Definition 4 | $\frac{(1 + 2\xi_i)}{(\xi_i + \xi_i^2)^{1-p}}, \quad 0 < p < 1$ |
| Definition 5 | $\frac{1 + \xi_i^p}{\xi_i^{1+p}}, \quad 0 < p < 1$ |
| Definition 6 | $\begin{matrix} 1 & \text{if} \quad i \in \Gamma_p \\ 0.001 & \text{otherwise} \end{matrix}, \quad 1 \leq p \leq n$ |
| Definition 7 | $\frac{1}{\mathbb{P}(Z_i \in \Gamma_p)}, \quad 1 \leq p \leq n$ |

an empirical characterization of $\gamma$. More precisely, given a training image, independent realizations of $X$ (denoted by $\bar{x}^{(1)}, \ldots, \bar{x}^{(L)}$) can be created from the computation (frequency counts) of higher order pattern statistics from the training image. Consequently, it can be assumed that these simulations follow an underlying distribution $\gamma$ that can be used to estimate $\xi_i$ by its empirical version

$$\hat{\xi}_i = \frac{1}{L} \sum_{l=1}^{L} |z_i^{(l)}|, \quad \forall i \in \{1, \ldots, n\}, \tag{8}$$

where $\bar{z}^{(l)} = (z_i^{(l)})_{i=1,\ldots,n}$ denotes the transform coefficients of $\bar{x}^{(l)}$.

## 4 Analysis of the Distribution of DCT Coefficients

Some evidence of the existence of persistent patterns in the transform domain (DCT) of the channelized fields is presented in this section. The multiple point simulation (MPS) algorithm *snesim* (Strebelle 2002) is adopted to simulate data from different image models. In principle, all simulated images conditioned on measurements honor the prior model. This implies that multiple-point patterns presented in the training image are reproduced on the simulations, and consequently, they present a common spatial structure in terms of orientation and complexity. The hypothesis is that this common structure in the spatial domain can be reflected in a persistent representation in the DCT transform domain across the simulations. Thus, the statistical information of the training image can be transformed into signal information by analyzing the trend of the transform coefficients on average.

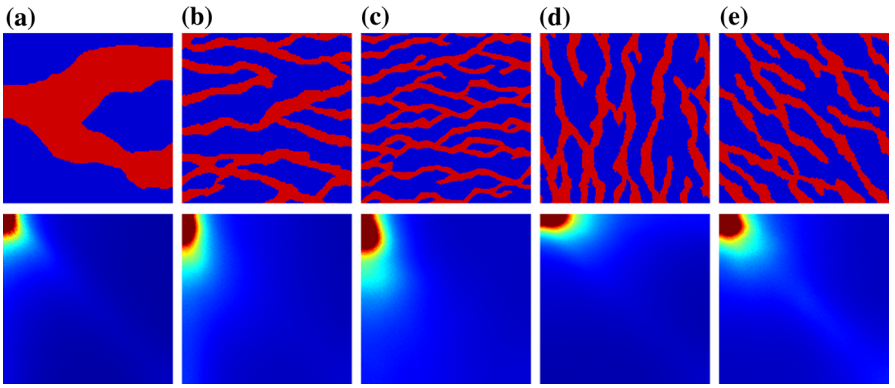


**Fig. 3** Average magnitude distribution of DCT transform coefficients from 1000 images. Models: monochannel (**a**), two horizontal multichannels (**b**, **c**), vertical and diagonal multichannels (**d**, **e**). Top: example from the database. Bottom: Average transform coefficients

For this analysis, three channelized models are considered (illustrated in the first row of Fig. 3) from a monochannel structure to a complex multichannel structure. To guarantee good statistical analysis, 1000 realizations were used for each model. Transform representations are computed from the data and for each model the average magnitude of transform coefficients is estimated as indicated in Eq. (8). The second row of Fig. 3 shows the average magnitude of the DCT representation for each model. Overall, it is clear that most of the energy is concentrated at low frequencies (upper left corner of the DCT image). While high frequencies describe facies transitions, most of the channel structure is captured by low frequencies information in a persistent location. In general, the probability of having a non-zero transform coefficient in a given low frequencies range is high, while outside this region the probability of having a significant (non-zero) coefficient decreases rapidly to zero.

In addition, the spatial distribution of average transform coefficients in Fig. 3 sheds some lights on the orientation and complexity of the field. If the channel structure presents a horizontal orientation, facies transitions occur in vertical direction, and, consequently, vertical frequencies appear as relevant elements of the average DCT representation (Fig. 3a–c). Analogously, the behavior of vertical structures is shown in Fig. 3d. In the case of fields that have diagonal orientations, the average DCT representation has no preferential directions and tends to be symmetric (Fig. 3e).

Finally, the channel complexity can be considered proportional to the number of facies transitions in a given orientation. The higher the facies transition rate, the larger the magnitude of the high frequency components in that orientation. Thus, more complex structures, in terms of geological features, present a larger number of significant coefficients in the DCT domain (in average). This explains why the average DCT signature illustrated in Fig. 3c contains more high frequency components than the average distribution presented in Fig. 3a–b.

The next section is devoted to evaluating the performance of the weighted CS (WCS) framework in (5) adopting the different options of weights presented in Sect. 3.2.

## 5 Reconstruction Results

This section is devoted to evaluating the facies reconstruction performance of the WCS method elaborated in Sect. 3 and comparing it with techniques that are based on pure CS algorithms, multiple-point simulations (MPS) and indicator kriging (IK). The main objective is to validate if the combined use of signal and statistical information (training image) can improve upon the use of each information source in isolation when the objective is image recovery. For this analysis, the same three facies models (from a simple monochannel structure to a rich multichannel structure) are considered to explore the performance of WCS in different complexity regimes.

*Snesim* (Strebelle 2002) data and pixel-domain information are combined for the WCS method. *Snesim* data are used to create a collection of channelized two-facies images. In particular, 1000 images of $200 \times 200$ pixels (pp) are created for each of the three models presented in the first row of Fig. 3a–c). With these data, the weights in Eq. (5) are estimated using the information of the average magnitude of the transform coefficients, as explained in Sects. 3.2 and 4. As seen in Fig. 1b, in the pixel-domain, samples are taken randomly with a uniform distribution, and the analysis is focused on the very low under-sampling range [0.1–2%] of measurements. The DCT basis is used to provide sparse representations as explained in Sect. 2.1.

In this work the ability of the methods to recover the original image is evaluated. The metrics adopted to recover the original image correspond to the standard signal-to-noise ratio (SNR) and the similarity structural index (SSIM) (Zhou et al. 2004). Finally, the obtained results are orientation invariant; hence, for the purposes of brevity only the analysis for the reconstruction of images with left-to-right channel orientation is presented.

### 5.1 Analysis of the Weights

To evaluate the performance of the WCS for the different weight definitions in Sect. 3.2, the reconstruction algorithm in Eq. (5) is applied, adopting the definitions presented in Table 1. Performances are evaluated in average with respect to realizations of the sensing modality for different data-rate regimes. For all definitions, only the results for the choice of $p$ that provide the best performance are presented.

Figure 4 illustrates these results for the three image models studied in this work. Overall, there is no particular definition for matrix $W$ that performs better than the others, and they all provide similar performance trends. This can be explained as the weights definitions present similar monotonic structures. An interesting observation is that the performance trend of the different weighting definitions are persistent across the models such that the definitions that have better performance are the same for the three facies structures. Finally, definition 1 with $p = 0$ provides the best results and is the one used for the rest of the experiments.

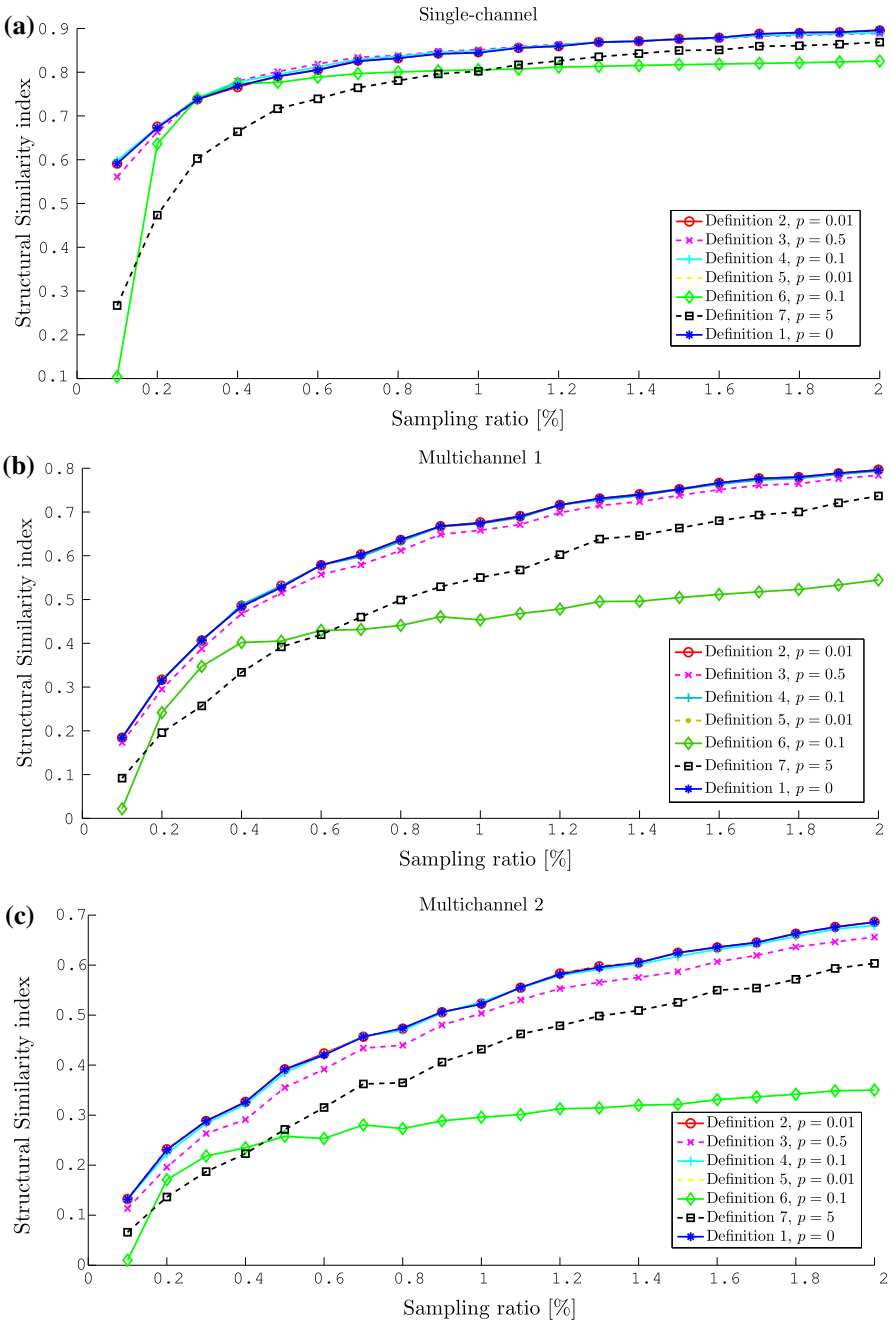


**Fig. 4** SSIM index performance for different weighting matrix $W$, performed from 25 realizations of the sensing matrix $A$. **a** Monochannel, **b** Multichannel 1 and **c** Multichannel 2. Each curve represents a particular definition in Table 1 using the best parameter $p$

### 5.2 Average Inter-block Reconstruction

In this section the evaluation of the *average inter-block CS* (AICS) approach (Calderon et al. 2015) is performed in the context of weighted CS. The basic idea of AICS is to decompose the image in non-overlapping square blocks and then apply the recovery algorithm, in this case the WCS, individually in each block. This block-by-block approach is performed sequentially for different block sizes (from $40 \times 40$ to $200 \times 200$ pp) creating a collection of reconstructions (Fig. 5). The next step is to compute the average image (pixel-by-pixel) across the solutions obtained for the different block sizes. Finally, a two-level hard thresholding is applied in the resulting image to obtain a binary result. This last step is conducted to match the categorical nature of the facies. The threshold is selected and applied at each pixel with the objective of preserving the proportion of high and low values observed on the measurements. Figure 5 shows examples of the intermediate block-by-block reconstructions for block-sizes $40 \times 40$ and $100 \times 100$, as well as the average inter-block reconstruction with and without the hard-thresholding. Here, the reconstructions for the monochannel model were recovered with 0.4% of measurements, the reconstructions of the multichannel 1 with 0.7% of measurements and the reconstructions of the multichannel 2, with 1%.

Figure 6 shows the performance of the block-by-block WCS approach for different block sizes, as well as the average inter-block WCS reconstruction with and without the final hard-thresholding step. For the three models, in the process of increasing the size of the block, the performance improves. This is justified since in the process of increasing the block, the channelized images become more compressible in the DCT domain (Calderon et al. 2015). In terms of the average reconstruction, this image

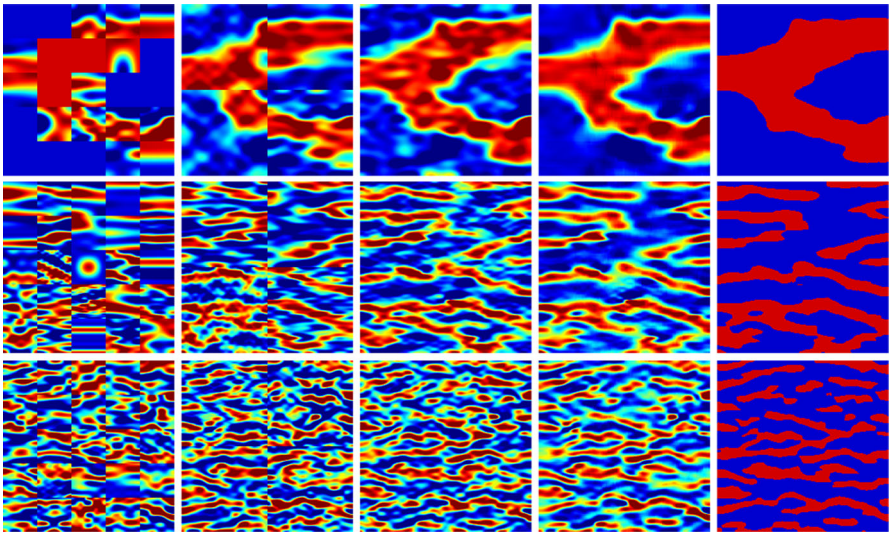

**Fig. 5** Illustration of recoveries from the WCS method as a function of block-size. From left to right: $40 \times 40$, $100 \times 100$ pp, full image, average image and average after thresholding. From top to bottom: monochannel, multichannel 1 and multichannel 2

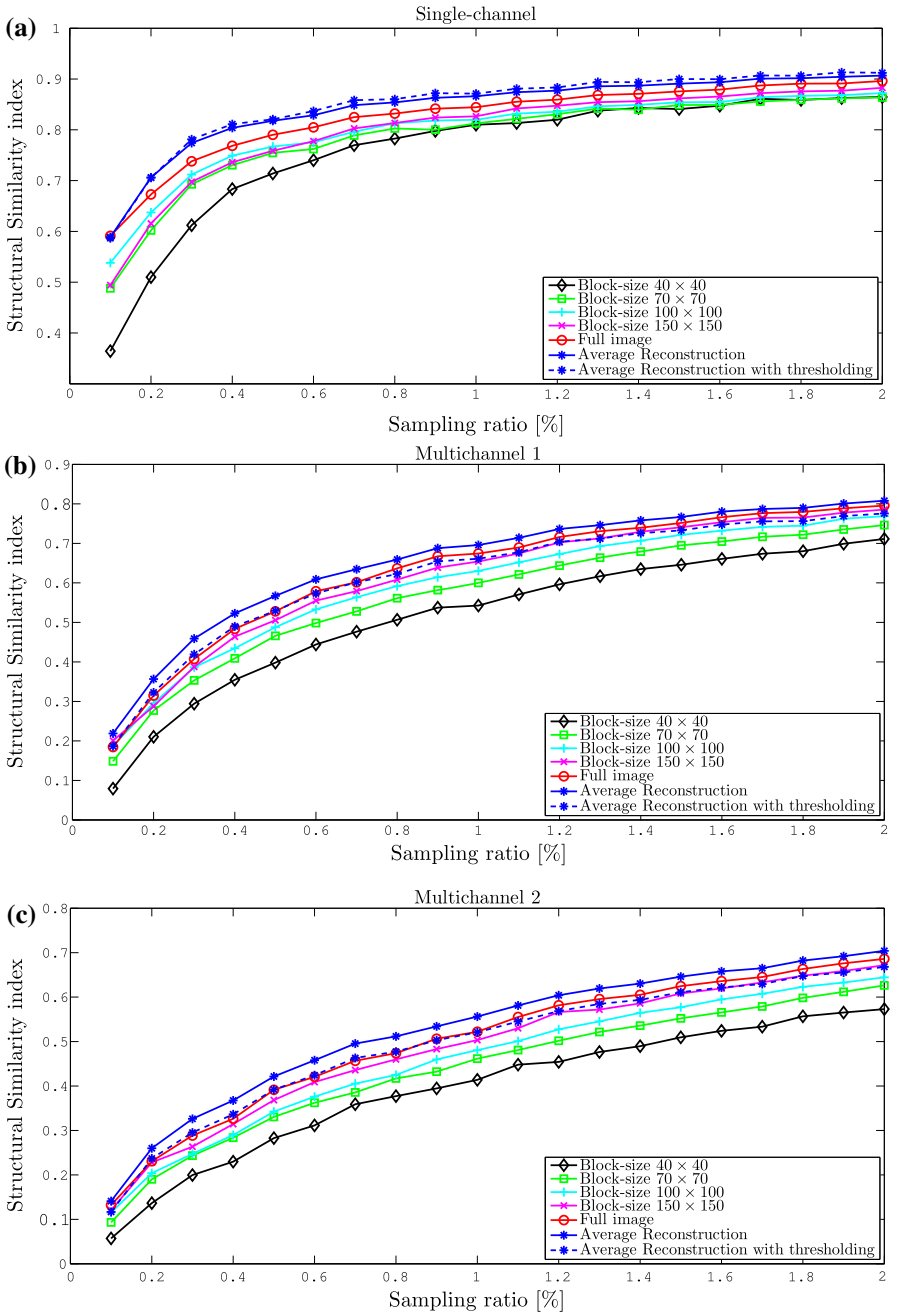


**Fig. 6** Performance of WCS as a function of the block-size in terms of SSIM index. Performance for: **a** monochannel, **b** multichannel 1 and **c** multichannel 2 model. Recovery images are performed from 25 realizations of the sensing matrix $A$

integrates information at different scales (block sizes), and it provides a performance gain with respect to the WCS method acting on the full image. This gain can be attributed to the fact that persistent features across different scales prevail, including orientation, complexity and dominant channel structures. As a consequence, these common features are accentuated while the artifacts of the particular recovered fields are mitigated.

In the final hard-thresholding stage, however, it is not possible to provide a unified conclusion for the three models. A separated analysis is needed for the monochannel and multichannel case. The hard-thresholding honors the proportion of low and high values in the samples and does not impose any channel features, such as connectivity, orientation and complexity. Therefore, in the multichannel case, the continuous and interconnected structure is not preserved after the hard-thresholding process, and consequently, the quality of the image is deteriorated. In fact, the SSIM index compares three quality features in the images: luminosity, contrast and structures (Zhou and Sun 1999). While the luminosity presents an enhancement after the hard-thresholding, the factors associated to contrast as well as structure are deteriorated. As a result, the perceptual quality in terms of the SSIM index deteriorates as a whole. This can be observed in the last two rows of Fig. 5. Many authors have dealt with this problem suggesting different approaches to correct these discontinuities (Strebelle and Remy 2004; Suzuki and Strebelle 2007; Shahraeeni 2019). Although some of these solutions are not directly applicable in this context, as the proposed approach does not perform simulation in a sequential manner, further research is needed to impose connectivity during the reconstruction. Post-processing the final reconstruction (Strebelle and Remy 2004) is one approach that may impose the expected connectivity.

In contrast, for the case of monochannel structures, the hard-thresholding process leads to an increase in the quality of the recovered images. Monochannel structures are simpler in terms of facies transitions and details. Then, with limited data the weighted CS solution is able to correctly estimate the dominant channel structure and low frequency information due to the persistent information of the energy distribution presented in the weighting matrix $W$ (Fig. 3). This knowledge constitutes an important fraction of the recovered field in the case of monochannel structures, which is not the case for multichannel models. Therefore, by applying the hard-thresholding, the large-scale interconnected structure obtained by the algorithm is preserved and, as a result, the quality of the recovered image increases due to the binary nature of the monochannel model. The first row of Fig. 5 illustrates this observation when recovering a monochannel facies (see the last two images at the right).

In summary, the average inter-block reconstruction provides an important improvement in the performance of the WCS approach, though the final hard-thresholding offers a marginal gain only for the case of monochannel model. In the next section, the best obtained inter-block WCS solutions for each channel model will be considered.

### 5.3 Evaluating the Sensing Variability and Comparison with Other Methods

This final section is devoted to evaluating the variability in the reconstruction of the optimized WCS approach obtained for each channel model (monochannel and multichannels). This variability occurs because the sensing matrix $A$ in Eq. (5) is a random object and, consequently, it is important to evaluate how robust the average inter-block WCS reconstruction is with respect to variations in the sensing modality (attributed to the selection of random pixels). This analysis is done as a function of the data rate regime. For that, the challenging under-sampling range from 0.1 to 2% of pixel-based data is explored, considering 25 realizations of the random matrix $A$ to compute average performances and standard deviations.

In this context, the performance of the proposed average inter-block WCS (AIWCS) is compared with the classical CS algorithm based on $\ell_1$-minimization (Candès et al. 2006a, b; Donoho 2006), the average inter-block CS approach (Calderon et al. 2015), the indicator kriging techniques (Deutsch and Journel 1998) and the multipoint algorithm *snesim* (Strebelle 2002). Although MPS is a method designed for simulation, it has been incorporated in this comparative analysis to illustrate that MPS can be a competitive alternative when the objective is the true image recovery.

Many observations can be made from Figs. 7 and 8, which show the trend of the average performance and standard deviation for all the evaluated methods as a function of the fraction of pixel-based measurement taken for reconstruction, using SSIM and SNR, respectively. Most importantly, for the three cases the proposed AIWCS shows an important improvement with respect to the average inter-block CS method, which does not take into account the statistical information from a training image or image model. For the monochannel case, the gain in performance is important in the sampling range from 0.2 to 0.8% for the SSIM index, while the gain is significant in all the sampling range for the SNR metric (Fig. 8).

Figure 9 presents some examples where the gains in recovery (with respect to the CS approach) can be clearly observed. For the case of multichannel facies models, the improvement is systematic and significant in the whole range explored and for the two fidelity indicators. Figures 10 and 11 show examples of recoveries for the case of multichannel models contrasting the proposed method with the average inter-block CS.

Another observation obtained from comparing these results is that, in terms of SSIM, MPS performs better than the pure CS-based solutions and the average inter-block CS strategy, methods that do not take into account the information of a training image. For the case of SNR indicator, MPS performs better than pure CS-based solutions for the monochannel case, while for the multichannel 1 and multichannel 2 scenarios, MPS shows better results than pure CS-based solutions in the regime beyond 0.5% and 0.9% samples, respectively.

When compared with indicator kriging (IK), which uses the same training model, MPS offers substantially better results (in SSIM and SNR) in all scenarios (channels) and sampling regimes. The only exception is for the scenario of monochannel in the (very small) regime of 0.1% and 0.2% samples, where IK shows better performances attributed to the simplicity of the monochannel model. This remarkable result provides a justification on the use of multiple point simulations from the perspective of image

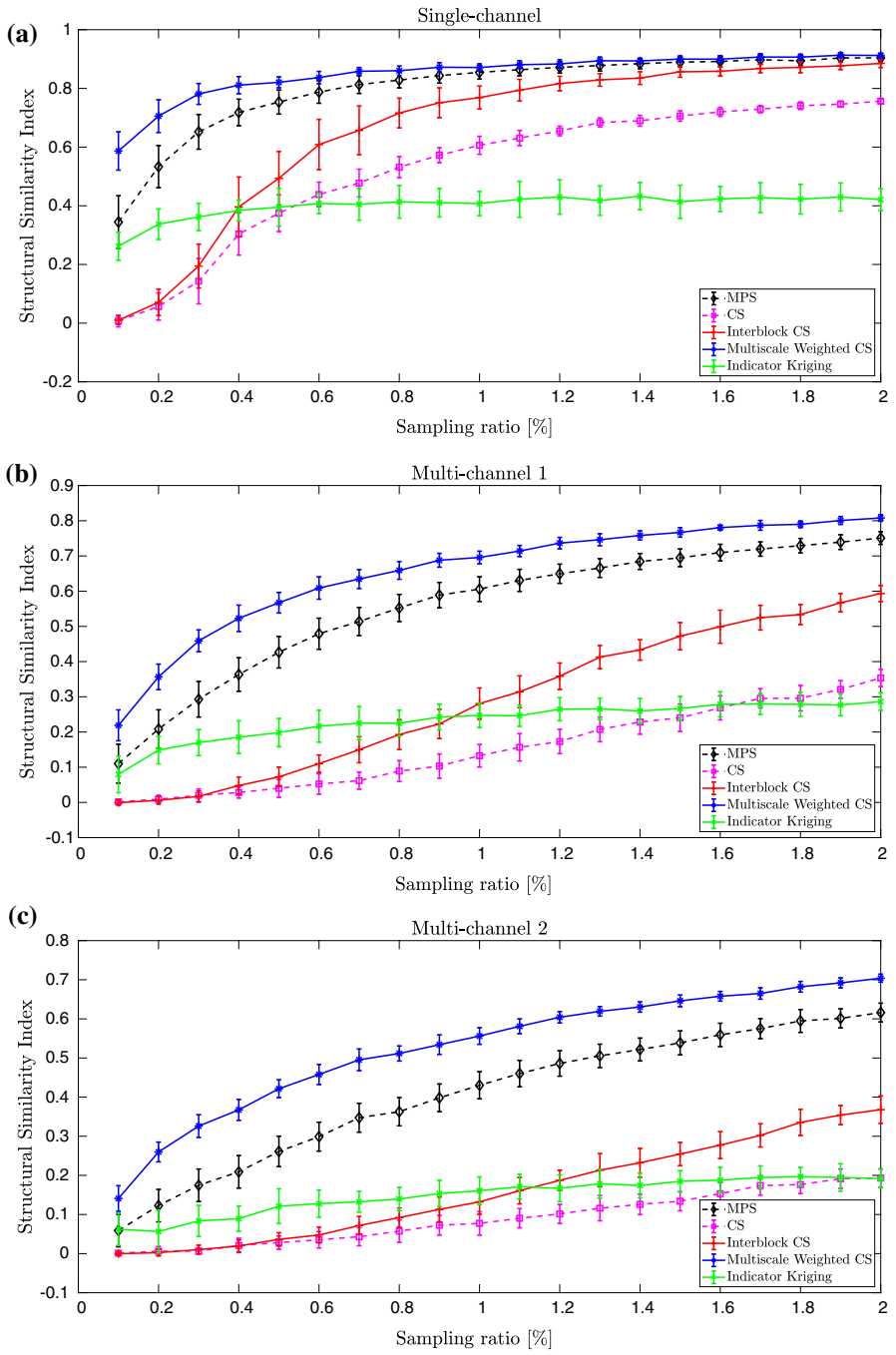


**Fig. 7** Average performance in terms of SSIM of the proposed WCS method, the inter-block CS method, the standard $\ell_1$-regularization, indicator kriging and multiple-points simulation. **a** Monochannel, **b** Multi-channel 1 and **c** Multichannel 2 model

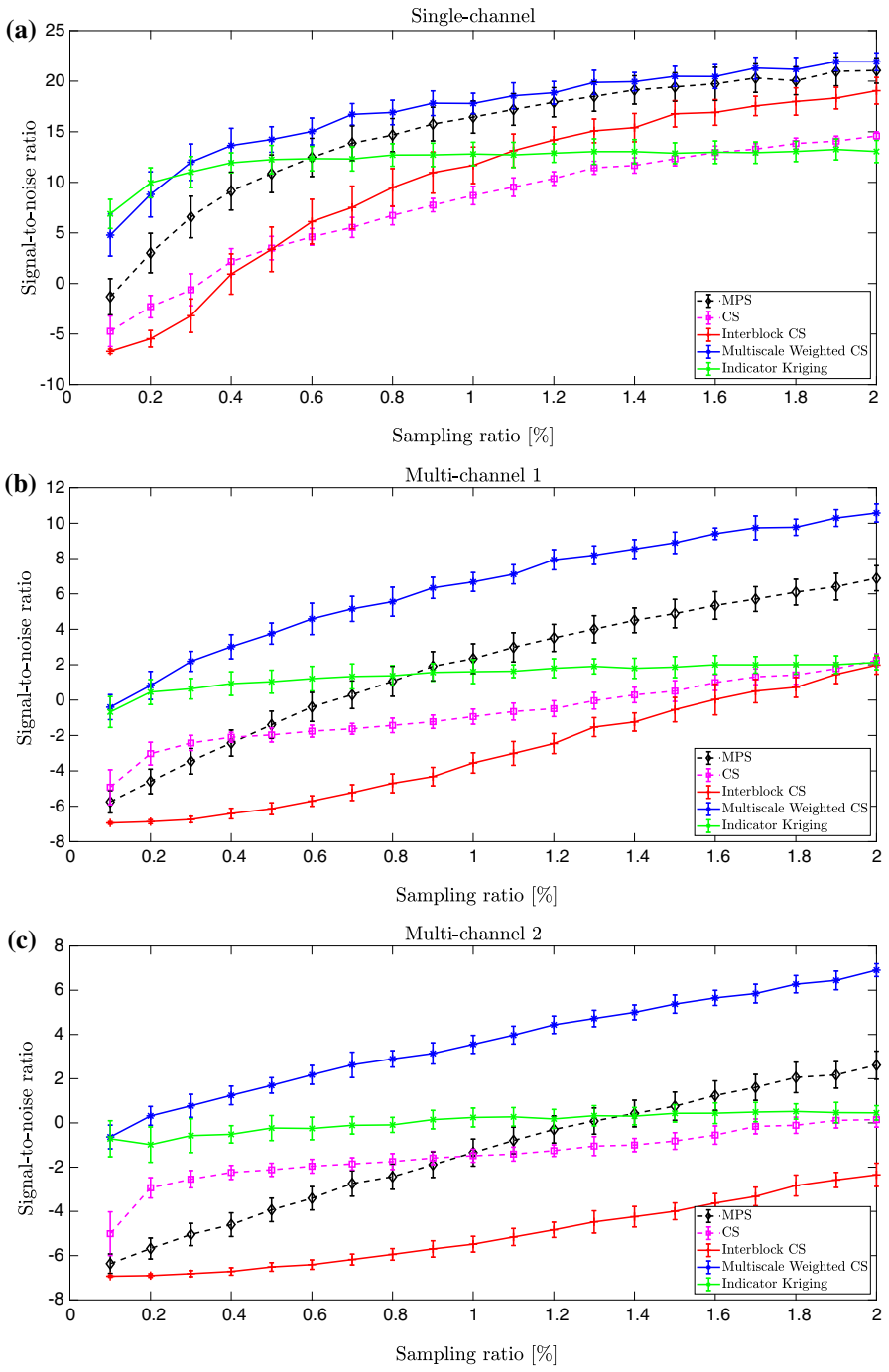


**Fig. 8** These are the same set of results presented in Fig. 7 but adopting the average SNR indicator as a fidelity measure to evaluate the quality of image recovery

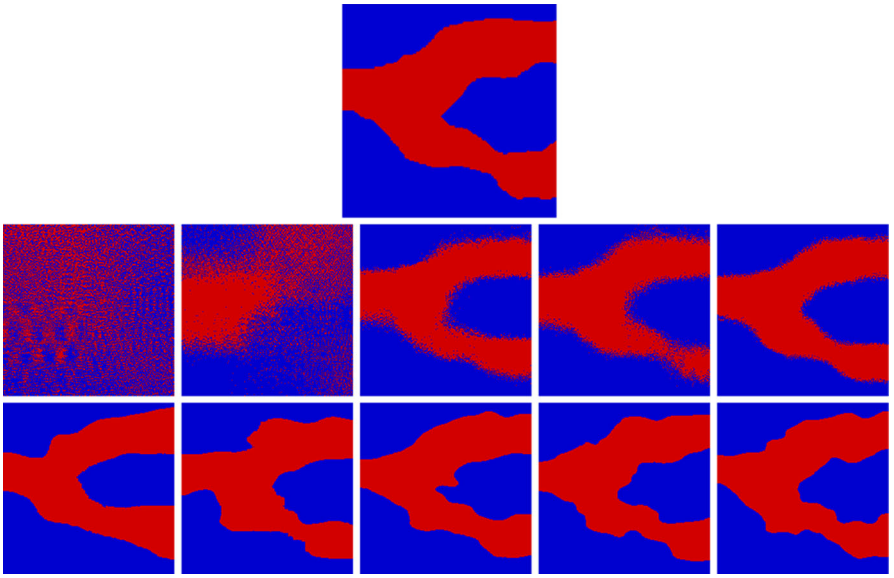

**Fig. 9** Graphic comparison between inter-block CS and weighted multi-scale CS, both with hard-thresholding post-processing. From left to right: Reconstruction from 0.1%, 0.2%, 0.5%, 0.7% and 1% of measurements. Top: Inter-block CS solver, Bottom: Weighted CS method

reconstruction as a very competitive alternative when compared with our proposed AIWCS method.

Finally, it is interesting to note that the proposed AIWCS outperforms MPS and IK in all the explored sampling range and for the three facies models. Again, for the case of monochannel model, the difference in performance is significant in the range [0.3–0.8%] and for the multichannel models the improvements are consistent throughout the sampling range explored. Therefore, it is possible to conclude that imposing structure on the image would seem to be responsible for the improved performance obtained using the proposed method in comparison with the MPS and IK approaches. This weighted CS solution for Eq. (6), which combines a sparse image assumption in the DCT domain and the statistical model in the pixel domain, are apparently complementary and relevant to improve reconstruction performances for facies images.

## 6 Conclusions

In this work a new scheme for geological facies reconstruction based on weighted compressed sensing (WCS) is presented and evaluated. Experimental results (reconstruction for three type of facies models with different pattern complexities) show that the proposed WCS approach offers better recovery than methods reported in the literature based on pure CS.

These results support our initial hypothesis that prior knowledge from a training image can significantly improve the reconstruction of $\ell_1$-promoting solutions when less than 1% of direct data is available. In this under-sampling regime, the information

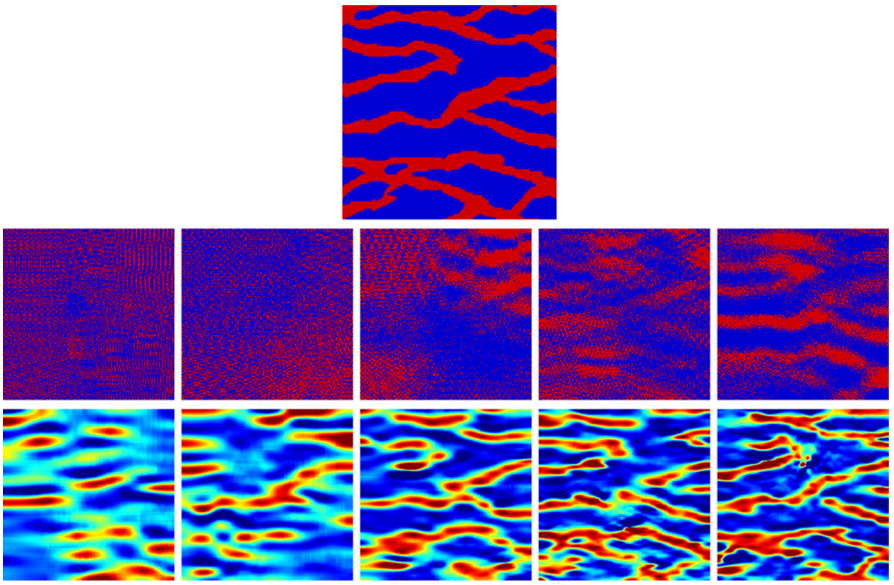

**Fig. 10** Same caption as Fig. 9 but analyzing the multichannel 1 model. In this case, the weighted CS method does not use a final hard-thresholding stage

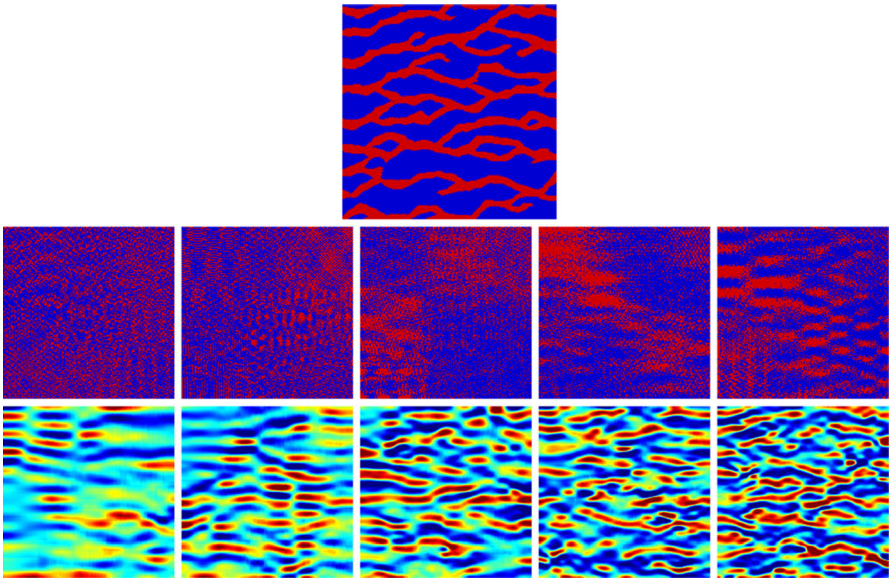

**Fig. 11** Same caption as Fig. 9 but analyzing the multichannel 2 model. In this case, the weighted CS method does not use a final hard-thresholding stage

from the data is so limited that prior knowledge plays a major role in improving the quality of the recovery as shown in Sect. 5.3. A practical consequence is that the proposed inter-block WCS method offers reasonable reconstruction in the range [0.2–

0.6%] of measurements, something that the original unweighted CS method was not able to achieve. From the authors perspective, these results show that $\ell_1$-promoting solutions that integrate both signal structure and statistical information (from a training image) can be a competitive alternative to MPS when the objective is true image recovery. Overall, the objective of image recovery with very limited data (less than 1% of the size of the image) is feasible for this type of channelized facies structures.

**Acknowledgements** The work was supported by the research Grants Fondecyt 1170854, CONICYT, Chile. The work of Dr. Silva is supported by the Advanced Center for Electrical and Electronic Engineering (AC3E), Basal Project FB0008. The work of Dr. Egaña is supported by the Advanced Mining Technology Center (AMTC) Basal project (CONICYT Project AFB180004). Felipe Santibañez is supported by CONICYT Ph.D. scholarship 21130890 and AMTC by the CONICYT Project AFB180004. Dr. Ortiz acknowledges the support of the Natural Sciences and Engineering Council of Canada (NSERC), funding reference number RGPIN-2017-04200 and RGPAS-2017-507956.

**Funding** Funding was provided by Fondo Nacional de Desarrollo Científico y Tecnológico (Grant Nos. 1170854, 1140840), Basal Project, Advanced Center for Electrical and Electronic Engineering (Grant No. FB0008), Comisión Nacional de Investigación Científica y Tecnológica (Grant Nos. 21130890, AFB180004) and Natural Sciences and Engineering Council of Canada (NSERC), funding reference number RGPIN-2017-04200 and RGPAS-2017-507956.

## Appendix A: The CS Recovery Theorem

For the problem presented in Sect. 2.1, the following result can be adopted to obtain performance guarantees for the recovery of $\bar{x}$ from $\bar{y}$ using sparsity as an assumption on $\bar{x}$.

**Theorem 1** (Candès and Plan 2011, Theorem 1.2) *For any $k < n$ and $\beta > 0$, with probability $1 - 6/n - 6e^{-\beta}$, the solution to Eq. (4) satisfies that*

$$\left|\left|\hat{x} - \bar{x}\right|\right|_{\ell_2} \leq \frac{C(1+\alpha)}{\sqrt{k}} \cdot ||\bar{z} - \tilde{z}_k||_{\ell_1}, \tag{9}$$

*provided that $m \geq C_\beta \cdot \mu(U) k \log n$, where*

$$\mu(U) = n \cdot \max_{i,j \in \{1,\ldots,n\}} \left|U_{i,j}\right|^2, \tag{10}$$

*$\tilde{z}_k \in \mathbb{R}^n$ is the best $k$-term approximation of $\bar{z}$, $\alpha = \sqrt{\frac{(1+\beta)k\mu \log n \log m \log^2 k}{m}}$, $C_\beta = (1+\beta)C_0$, and $C$ and $C_0$ numerical constants.*

Thus, if the signal is $k$-sparse in the transform domain $U$, that is, $||\bar{z} - \tilde{z}_k||_{\ell_1} = 0$, and the number of measurements satisfies that $m \geq C_\beta \cdot \mu(U) k \log n$, then $\hat{x} = \bar{x}$ from (9). Therefore, the sparsity assumption on $\bar{z}$ and the use of a critical number of measurements (that scales like $O(k \log n)$) guarantees perfect recovery for the $\ell_1$-minimizer scheme in (4).

## Appendix: Basis Selection

From Theorem 1, there are two elements to consider to address the problem of selecting $U$ optimally for the recovery of $\bar{x}$ from $\bar{y}$. On the one hand, $U$ should offer a good sparse representation of the facies images, in the sense that the approximation error $||\bar{z} - \tilde{z}_k||_{\ell_1} \approx 0$ for a small fraction of transform coefficients, that is for $k << n$. On the other hand, the number of required measurements in (10) is proportional to $\mu(U)$, which is an indicator of how coherent (or orthogonal) is $U$ with respect to the canonical (pixel-based) basis. Only looking at this second criterion, to minimize the number of measurements it is required a value of $\mu(U)$ close to 1, which is known to be the minimum value (coherent) that can be obtained for any pair of bases $A$ and $U$. Integrating the two criteria, there is a tradeoff between the compressibility quality of $U$, which is the ability of $U$ to represent $\bar{z} \equiv U^{\dagger}\bar{x}$ with a small proportion of coefficients, and how incoherent is $U$ with respect to the pixel-based domain. More precisely using the result in Theorem 1, for a basis $U$, a signal $\bar{x}$ and a target reconstruction error $\epsilon > 0$, the following object can be defined (Calderon et al. 2015)

$$k(\bar{x}, U, \epsilon) \equiv \min \left\{ 1 \leq k \leq n : \text{such that } \frac{C(1+\alpha)}{\sqrt{k}} \cdot \sigma_k(U^{\dagger}\bar{x})_{\ell_1} \leq \epsilon \right\}, \quad (11)$$

where $\sigma_k(\bar{z})_{\ell_1} = ||\bar{z} - \tilde{z}_k||_{\ell_1}$ is the approximation error introduced in (9). From Theorem 1, $k(\bar{x}, U, \epsilon)$ represents the critical number of significant (transform) coefficients (with respect to $U$) needed to have a reconstruction error smaller than $\epsilon$ [Eq. (9)].

Then, considering a collection of orthonormal bases $\{U_j, j \in J\}$, the optimal one from Theorem 1 is the one that requires the minimum number of measurements to achieve an error $\epsilon$, that is, the solution of

$$U^*(\epsilon, \bar{x}) = \arg \min_{U_j, j \in J} k(\bar{x}, U_j, \epsilon) \cdot \mu(U_j). \quad (12)$$

It is shown in (Calderon et al. 2015, Sect. 5) that over a rich collection of Wavelet bases, the discrete cosine transform (DCT) by far offers the best tradeoff between compressibility and incoherence to recover channelized facies from pixel-based measurements for the classical CS algorithm in (4). This was shown for different channelized facies models and reconstruction errors. Therefore, the DCT was the basis adopted in this work.

## References

Amizic B, Derin Babacan S, Molina R, Katsaggelos AK (2010) Sparse Bayesian blind image deconvolution with parameter estimation. In: European signal processing conference, pp 626–630. https://doi.org/10.1186/1687-5281-2012-20

Arpat B, Caers J (2007) Conditional simulations with patterns. Math Geol 39(2):177–203

Babacan SD, Molina R, Katsaggelos AK (2009) Variational Bayesian blind deconvolution using a total variation prior. IEEE Trans Image Process 18(1):12–26. https://doi.org/10.1109/TIP.2008.2007354

Blumensath T, Davies M (2009) Iterative hard thresholding for compressive sensing. Appl Comput Harmon Anal 27(7):265–274

Bogdan M, van den Berg E, Su W, Candes E (2013) Statistical estimation and testing via the sorted L1 norm. ArXiv e-prints arXiv:1310.1969

Bondell HD, Reich BJ (2008) Simultaneous regression shrinkage, variable selection, and supervised clustering of predictors with OSCAR. Biometrics 64:115–123. https://doi.org/10.1111/j.1541-0420.2007.00843.x

Calderon H, Silva JF, Ortiz JM, Egana A (2015) Reconstruction of channelized geological facies based on RIPless compressed sensing. Comput Geosci 77:54–65

Candès E, Plan Y (2011) A probabilistic and RIPless theory of compressed sensing. IEEE Trans Inf Theory 57(11):7235–7254

Candès E, Tao T (2005) Decoding by linear programming. IEEE Trans Inf Theory 51(12):4203–4215. https://doi.org/10.1109/TIT.2005.858979

Candès E, Tao T (2006) Near-optimal signal recovery from random projections: universal encoding strategies? IEEE Trans Inf Theory 52(12):5406–5425

Candès E, Romberg J, Tao T (2006a) Robust uncertainty principles: exact signal reconstruction from highly incomplete frequency information. IEEE Trans Inf Theory 52(2):489–509

Candès E, Romberg J, Tao T (2006b) Stable signal recovery from incomplete and inaccurate measurements. Commun Pure Appl Math 59:1207–1223

Candès E, Wakin M, Boyd S (2008) Enhancing sparsity by reweighted $\ell_1$ minimization. J Fourier Anal Appl 14(5–6):877–905. https://doi.org/10.1007/s00041-008-9045-x

Chen Z, Babacan SD, Molina R, Katsaggelos AK (2014) Variational Bayesian methods for multimedia problems. IEEE Trans Multimed 16(4):1000–1017. https://doi.org/10.1109/TMM.2014.2307692

Choudhary S, Mitra U (2014) Sparse blind deconvolution: what cannot be done. In: IEEE international symposium on information theory—proceedings, pp 3002–3006. https://doi.org/10.1109/ISIT.2014.6875385

Cohen A, Dahmen W, DeVore R (2009) Compressed sensing and best $k$-term approximation. J Am Math Soc 22(1):211–231

Deutsch CV, Journel AG (1998) GSLIB: geostatistical software library and user's guide, 2nd edn. Oxford University Press, New York

Donoho D (2006) Compressed sensing. IEEE Trans Inf Theory 52(4):1289–1306

Donoho DL, Vetterli M, DeVore RA, Daubechies I (1998) Data compression and harmonic analysis. IEEE Trans Inf Theory 44(6):2435–2476

Elad M (2010) Sparse and redundant representations, 1st edn. Springer, New York

Elsheikh A, Wheeler M, Hoteit I (2013) Sparse calibration of subsurface flow models using nonlinear orthogonal matching pursuit and an iterative stochastic ensemble method. Adv Water Resour 56:14–26

Fergus R, Singh B, Hertzmann A, Roweis ST, Freeman WT (2006) Removing camera shake from a single photograph. In: ACM SIGGRAPH 2006 Papers—SIGGRAPH '06, p 787. https://doi.org/10.1145/1179352.1141956

Figueiredo MAT, Nowak RD (2014) Sparse estimation with strongly correlated variables using ordered weighted L1 regularization. ArXiv e-prints arXiv:1409.4005

Guardiano F, Srivastava M (1993) Multivariate geostatistics: beyond bivariate methods. In: Geostatistics-Troia. Kluwer Academic, Amsterdam, pp 133–144

Huang J, Huang X, Metaxas D (2008) Simultaneous image transformation and sparse representation recovery. In: 2008 IEEE conference on computer vision and pattern recognition, pp 1–8. https://doi.org/10.1109/CVPR.2008.4587640

Jafarpour B (2011) Wavelet reconstruction of geologic facies from nonlinear dynamic flow measurements. IEEE Trans Geosci Remote Sens 49(5):1520–1535

Jafarpour B, McLaughlin DB (2009) Reservoir characterization with the discrete cosine transform. SPE J 14(1):182–201

Jafarpour B, Goyal VK, McLaughlin DB, Freeman WT (2009) Transform-domain sparsity regularization for inverse problems in geosciences. Geophysics 74(5):R69–R83

Jafarpour B, Goyal VK, McLaughlin DB, Freeman WT (2010) Compressed history matching: exploiting transform-domain sparsity for regularization of nonlinear dynamic data integration problems. Math Geosci 42(1):1–27

Ji G, Hughes MC, Sudderth EB (2017) From patches to images: a nonparametric generative model. In: Precup D, Teh YW (eds) Proceedings of the 34th international conference on machine learning, PMLR, Inter-

national Convention Centre, Sydney, Australia, Proceedings of Machine Learning Research, vol 70, pp 1675–1683. http://proceedings.mlr.press/v70/ji17a.html
Jung H, Jo H, Kim S, Lee K, Choe J (2017) Recursive update of channel information for reliable history matching of channel reservoirs using enkf with DCT. J Pet Sci Eng 154:19–37. https://doi.org/10.1016/j.petrol.2017.04.016. http://www.sciencedirect.com/science/article/pii/S092041051730428X
Jung H, Jo H, Kim S, Lee K, Choe J (2018) Geological model sampling using PCA-assisted support vector machine for reliable channel reservoir characterization. J Pet Sci Eng 167:396–405. https://doi.org/10.1016/j.petrol.2018.04.017. http://www.sciencedirect.com/science/article/pii/S0920410518303231
Khajehnejad M, Xu W, Avestimehr A, Hassibi B (2011) Analyzing weighted $\ell_1$ minimization for sparse recovery with nonuniform sparse models. IEEE Trans Signal Process 59(5):1985–2001. https://doi.org/10.1109/TSP.2011.2107904
Khaninezhad MR, Jafarpour B (2017) A discrete imaging formulation for history matching complex geologic facies. In: Society of petroleum engineers p 22. https://doi.org/10.2118/182727-MS
Khaninezhad MM, Jafarpour B (2014) Hybrid parametrization for robust history matching. SPE J 19(3):487–499
Khaninezhad MM, Jafarpour B, Li L (2012) Sparse geologic dictonaries for subsurface flow model calibration: part 1 inversion formulation. Adv Water Resour 39:106–121
Lee J, Kitanidis P (2013) Bayesian inversion with total variations prior for discrete geologic structure identification. Water Resour Res 49:7658–7669
Lee K, Jung S, Choe J (2016) Ensemble smoother with clustered covariance for 3D channelized reservoirs with geological uncertainty. J Pet Sci Eng 145:423–435. https://doi.org/10.1016/j.petrol.2016.05.029. http://www.sciencedirect.com/science/article/pii/S0920410516302005
Lee K, Lim J, Choe J, Lee HS (2017) Regeneration of channelized reservoirs using history-matched facies-probability map without inverse scheme. J Pet Sci Eng 149:340–350. https://doi.org/10.1016/j.petrol.2016.10.046. http://www.sciencedirect.com/science/article/pii/S0920410516308178
Leuangthong O, McLennan J, Deutsch C (2004) Minimum acceptance criteria for geostatistical realizations. Nat Resour Res 13(3):131–141
Li L, Jafarpour B (2009) An iteratively reweighted algorithm for sparse reconstruction of subsurface flow properties from nonlinear dynamic data. CoRR abs/0911.2270, arXiv:0911.2270
Likas AC, Galatsanos NP (2004) A variational approach for Bayesian blind image deconvolution. IEEE Trans Signal Process 52(8):2222–2233. https://doi.org/10.1109/TSP.2004.831119
Mallat S (2009) A wavelet tour of signal processing, 3rd edn. Academic Press, New York
Mallat S, Zhang Z (1993) Matching pursuit with time-frequency dictionaries. IEEE Trans Signal Process 41(12):3397–3415
Mariethoz G, Caers J (2015) Multiple-point geostatistics. Wiley, Hoboken
Mariethoz G, Lefebvre S (2014) Bridges between mutiple-point geostatistics and texture synthesis: review and guidelines for future research. Comput Geosci 66:66–80
Mariethoz G, Renard P (2010) Reconstruction of incomplete data sets or images using direct sampling. Math Geosci 42:245–268
Minniakhmetov I, Dimitrakopoulos R, Godoy M (2018) High-order spatial simulation using legendre-like orthogonal splines. Math Geosci 50:753–780
Miskin J, MacKay D (2001) Ensemble learning for blind source separation. In: Principles and practice, independent component analysis, pp 209–233
Molina R, Katsaggelos A, Abad J, Mateos J (1997) A Bayesian approach to blind deconvolution based on Dirichlet\ndistributions. In: 1997 IEEE international conference on acoustics, speech, and signal processing 4:2809–2812. https://doi.org/10.1109/ICASSP.1997.595373
Ortiz JM, Deutsch CV (2004) Indicator simulation accounting for multiple-point statistics. Math Geol 36(5):545–565
Peredo O, Ortiz JM (2011) Parallel implementation of simulating annealing to reproduce mutliple-point statistics. Comput Geosci 37:1110–1121
Perrone D, Favaro P (2014) Total variation blind deconvolution: the devil is in the details. In: Proceedings of the IEEE computer society conference on computer vision and pattern recognition, pp 2909–2916. https://doi.org/10.1109/CVPR.2014.372
Perrone D, Favaro P (2016) A clearer picture of total variation blind deconvolution. IEEE Trans Pattern Anal Mach Intell 38(6):1041–1055. https://doi.org/10.1109/TPAMI.2015.2477819. arXiv:1412.0251

Rudin LI, Osher S, Fatemi E (1992) Nonlinear total variation based noise removal algorithms. Phys D: Nonlinear Phenom 60(1–4):259–268. https://doi.org/10.1016/0167-2789(92)90242-F. arXiv:1011.1669v3

Sana F, Katterbauer K, Al-Naffouri T, Hoteit I (2015) Enhanced recovery of subsurface geological structures using compressed sensing and the ensemble kalman filter. In: 2015 IEEE international geoscience and remote sensing symposium (IGARSS), pp 3107–3110. https://doi.org/10.1109/IGARSS.2015.7326474

Sana F, Katterbauer K, Al-Naffouri TY, Hoteit I (2016) Orthogonal matching pursuit for enhanced recovery of sparse geological structures with the ensemble kalman filter. IEEE J Sel Top Appl Earth Obs Remote Sens 9(4):1710–1724. https://doi.org/10.1109/JSTARS.2016.2518119

Shahraeeni M (2019) Enhanced multiple-point statistical simulation with backtracking, forward checking and conflict-directed backjumping. Math Geosci 51(2):155–186. https://doi.org/10.1007/s11004-018-9761-y

Srinivas U, Suo Y, Dao M, Monga V, Tran TD (2015) Structured sparse priors for image classification. IEEE Trans Image Process 24(6):1763–1776. https://doi.org/10.1109/TIP.2015.2409572

Strebelle S (2002) Conditional simulation of complex geological structures using multiple points statistics. Math Geol 34(1):1–22

Strebelle S, Remy N (2004) Post-processing of multiple-point geostatistical models to improve reproduction of training patterns. In: Geostatistics Banff 2004, vol 2, pp 979–988

Suzuki S, Strebelle S (2007) Real-time post-processing method to enhance multiple-point statistics simulation. In: Petroleum geostatistics 2007

Tahmasebi P, Sahimi M, Caers J (2014) Ms-CCSIM: accelerating pattern-based geostatistical simulation of categorical variables using multi-scale search in Fourier spaces. Comput Geosci 67:75–88

Tahmasebi P, Sahimi M, Andrade JE (2017) Image-based modeling of granular porous media. Geophys Res Lett 44:4738–4746

Tan X, Tahmasebi P, Caers J (2014) Comparing training-image based algorithms using an analysis of distances. Math Geosci 46:149–169

Tropp J, Gilbert A (2007) Signal recovery from random measurements via orthogonal matching pursuit. IEEE Trans Inf Theory 53(12):4655–4666

Vega M, Molina R, Katsaggelos AK (2014) Parameter estimation in Bayesian blind deconvolution with super Gaussian image priors. In: European signal processing conference. https://doi.org/10.1016/j.ijhm.2015.04.012

Vetterli M, Kovacevic J (1995) Wavelet and subband coding. Prentice-Hall, Englewood Cliffs

Wang Y, Arns CH, Rahman SS, Arns JY (2018) Porous structure reconstruction using convolutional neural networks. Math Geosci 50:781–799

Wu J, Boucher A, Zhang T (2008) A SGeMS code for pattern simulation of continuous and categorical variables: FILTERSIM. Comput Geosci 34(12):1863–1876

Xu Y, Yin W (2016) A fast patch dictionary method for whole image recovery. Inverse Probl Imaging 10(2):563. https://doi.org/10.3934/ipi.2016012, http://aimsciences.org//article/id/f83bb625-c5c0-4bd6-a828-b6c548abaadb

Zeng X, Figueiredo M (2014) The atomic norm formulation of oscar regularization with application to the Frank-Wolfe algorithm. In: 2014 Proceedings of the 22nd European signal processing conference (EUSIPCO), pp 780–784

Zhang Y, Kuo Hw, Wright J (2018) Structured local minima in sparse blind deconvolution. In: Advances in neural information processing systems, pp 2328–2337

Zhao Y, Li D (2012) Reweighted $\ell_1$-minimization for sparse solutions to underdetermined linear systems. SIAM J Optim 22(3):1065–1088. https://doi.org/10.1137/110847445

Zhou X, Sun W (1999) On the sampling theorem for wavelet subspaces. J Fourier Anal Appl 5(4):347–354

Zhou W, Bovik A, Sheikh H, Simoncelli E (2004) Image quality assessment: from error visibility to structural similarity. IEEE Trans Image Process 13(4):600–612

Zhou X, Molina R, Zhou F, Katsaggelos AK (2014) Fast iteratively reweighted least squares for lpregularized image deconvolution and reconstruction. In: 2014 IEEE international conference on image processing, ICIP 2014, pp 1783–1787. https://doi.org/10.1109/ICIP.2014.7025357